Nanoscale

Accepted Manuscript

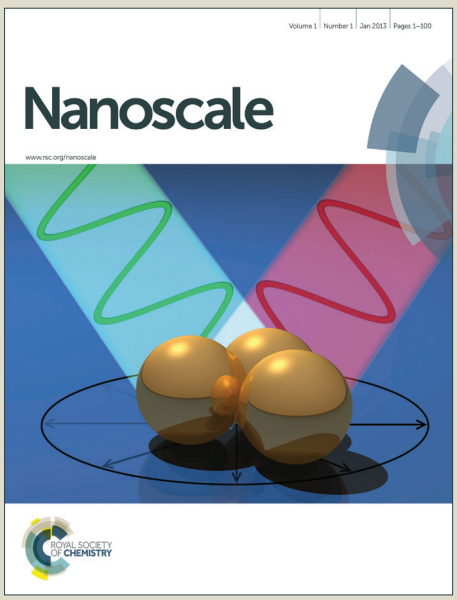

ROYAL SOCIETY OF CHEMISTRY

www.rsc.org/nanoscale

Nanoscale

RSCPublishing

ARTICLE

Phase-segregated Pt-Ni Chain-Like Nanohybrids with High Electrocatalytic Activity towards Methanol Oxidation Reaction

Cite this: DOI: 10.1039/x0xx00000x

Lili Wang, Dongfeng Zhang* and Lin Guo*

Received 00th January 2013,
Accepted 00th January 2013

DOI: 10.1039/x0xx00000x

www.rsc.org/

The phase-segregated Pt-Ni chain-like nanostructures, composed by the attachment of the monometallic counterparts, were synthesized via a modified polyol process with the assistance of small amount of PVP. The molar ratio between Pt and Ni were tuned by simply adjusting the feed ratio of the precursors. High-resolution transmission electron microscopy (HR-TEM) and X-ray photoelectron spectroscopy (XPS) results reveal that atomic diffusion occurred at the interface of the granular subunits. The negatively shift of the $Pt4f_{7/2}$ peak in the XPS spectra indicates the electron transfer from Ni to Pt atoms, while the strong peaks at around 855.7 eV suggests the surface oxidation of the Ni nanoparticles, which was further confirmed by the cyclic voltammetry (CV) measuremen. The electrocatalytic activities for the methanol oxidation reaction (MOR) were found higher for the phase-segregated structures relative to that of pure Pt nanoparticles, and the activities followed the sequences of Pt_1Ni_1> Pt_3Ni_1~Pt_2Ni_3 >> pure Pt. We believe the modified electronic structures and the existence of nickel hydroxide both contributed to the improved catalytic activities.

Introduction

Direct methanol fuel cells (DMFC), with the advantages of high energy conversion efficiency, safe storage and less pollution, is expected as one of the promising candidates used in small portable electronic products. Platinum is still the most effective anode electrocatalyst towards the methanol oxidation reaction (MOR). However, the high cost and low tolerance to carbon monoxide (CO) of pure Pt catalysts are the main drawback hindering the widespread application of this technology.[1-3]

Since researchers found that deposition of Pt nanoparticles on transition metals (TM) could significantly enhance the CO tolerance and considerably improve the catalytic activity for MOR,[4-6] Pt-based bimetallic catalysts have received great research attention. An electronic effect was proposed to explain the enhancement. The theory deems that the d-band position of Pt is lowered owing to the modified electronic structure by the electron transfer from the TM substrates to the Pt overlayers.[7-9] According to the Hammer-Nørskov model, the binding energy of CO on the metallic catalyst is proportional to the d-band center of the surface atoms.[10, 11] Thus, it is reasonable to expect the weakened adsorption of CO on Pt with the downshifted d-band center. Furthermore, studies also revealed that the monolayer-dispersed Pt on the substrate would maximize the electronic modification.[7, 12]

The amazing results triggered the research on Pt-based bimetallic nanoalloys[13-16] to mimic the electronic and catalytic properties established on extended surfaces. Further researches show that besides the electronic effect between TM and Pt, the existence of TM hydroxides might also play an important role in improving the electrocatalytic activity towards MOR, because the hydroxides have high electronic conductivity and can innately express OH species to remove the Pt-adsorbed CO.[17-19]

However, the alloy structure will inevitably block the formation of the hydroxide.[20] Hence, in the past several years, there has been a debate on which is more important for the improved performance, alloying or the existence of hydroxide.[21-23] For example, Lu and co-workers[24] showed that both increase the content of hydrous ruthenium oxides and decrease the particle size were all benefit for the catalytic activity, whereas the effect of the alloy degree turned out to be unremarkable. Long et al.[20] even proposed that avoiding the formation of PtRu bimetallic alloys could make the catalysts more active for MOR, because they believed that the RuO_xH_y speciation in nanoscaled Pt-Ru blacks afforded much more active sites than Ru^0 did as part of the bimetallic alloy. Park and collaborates also attributed isolated monometallic NPs as the active composition in Pt-Ni[25] and Pt-Co[26] nanohybrids for CO PROX. Inspired by these results, it is reasonable to conclude that a structure containing both intimately interacted Pt/TM interface and TM hydroxides would have optimized catalytic activity.

In addition, most Pt-based bimetallic nanocatalysts were prepared using organometallic precursors (such as acetylacetonate) in the high-boiling organic solvent up till now.[27-29] On the one hand, it would do great harm to both human body and environment. On the other hand, the residue from these organic molecules, which cannot be easily removed, might block the surface reactive sites and thus deactivating the catalyst.[30, 31]

By sharing this insight, we report the fabrication of phase-segregated Pt-Ni chain-like structures composed by the attachment of the nanoscaled monometallic counterparts in ethylene glycol solution with the assistance of a small amount of Polyvinyl Pyrrolidone (PVP). The atomic diffusion at the interface guaranteed the modification of the electronic structure of Pt via electron transfer, while the phase-segregated structure made it possible to generate sufficient nickel hydroxides. The electrochemical

measurement confirms that the phase-segregated structures possessed much higher catalytic activities towards MOR relative to pure Pt nanocatalysts.

Experimental

The phase-segregated Pt-Ni bimetallic nanocrystals were prepared through a separated reduction procedure via a modified polyol process. Ethylene glycol served as both the reducing agent and the solvent. Typically, 0.0292g K_2PtCl_6 and 0.0260g PVP were dissolved into 30mL ethylene glycol. Then, appropriate amount of $NiCl_2{\cdot}6H_2O$ was introduced into the above mixture to obtain bimetallic nanocrystals with different Pt/Ni molar ratio. After stirring for 30 minutes, a homogeneous transparent solution formed. After the temperature was raised to the boiling point (~190°C), 3.0 mL solution containing 0.2 mL 80% hydrazine hydrate ($N_2H_4{\cdot}H_2O$) and 2.8 mL ethylene glycol was added into the above mixture. It was allowed to keep refluxing for 2 hours to complete the reaction. After the mixture was cooled to room temperature, the produced precipitates were collected by centrifugation and washed with ethanol for several times. All the experimental procedures were performed open to the atmosphere. And all the reagents were used without further purification.

The crystalline structures of the as-synthesized products were analyzed by X-ray diffraction (XRD) recorded on a Rigaku D/max-2200 diffractometer employing Cu-Kα radiation (λ = 1.54056 Å) at a scanning rate of 0.01 deg/s ranging from 30 to 90°. The morphologies were investigated by the transmission electron microscope (TEM) and high-resolution TEM (HR-TEM) on a JEOL instrument (JEM-2100F) working at 200kV. The composition of the as-synthesized Pt-Ni nanocatalysts were characterized by energy dispersive X-ray spectroscopy (EDX) equipped within the JEM-2100F TEM. XPS analyses were performed on an AXIS-Ultra instrument using monochromatic Al Kα radiation with 1486.71 eV operated at 15kV and 225W. To compensate for surface charges effects, binding energies were calibrated using C 1s hydrocarbon peak at 284.80 eV.

The electrochemical measurements were performed in a standard three-electrode cell at room temperature conducted with a CHI660C electrochemical workstation (Chenhua, Shanghai). A Pt wire was used as the counter electrode, and an Ag/AgCl electrode saturated with KCl was used as the reference electrode. The working electrode was prepared as follows. An aliquot of 5 μL of 2 mg/mL as-synthesized nanocatalyst suspension in deionized water was dropped onto the glassy carbon electrode (3 mm in diameter), which was polished smoothly and washed cleanly in advance. After the water evaporated completely, 5μL of the 0.2 mol/L Nafion as a binding agent was cast on the top of the catalyst layer. The coated working electrode was then dried completely in air. The cyclic voltammetry (CV) measurements were carried out in the aqueous solution of 0.5mol/L H_2SO_4 with or without 1mol/L CH_3OH for different purposes. Chronoamperometry measurements were performed under a potential of 0.7V for 600 s in 0.5 mol/L H_2SO_4 + 1.0 mol/L CH_3OH solution. All solutions were fully purged with Ar gas before the measurements.

Results and discussion

The phase-segregated Pt-Ni bimetallic nanohybrids with adjusted molar ratio were prepared through a separated reduction procedure via a modified polyol process. Figures 1(a) to 1(c) display the typical TEM images of the as-synthesized products with different Pt/Ni atomic ratios. The inserted tables illustrate that the average Pt/Ni atomic ratios in different electrocatalysts were 2.89:1, 1.15:1 and 0.63:1, approaching to the average molar ration of Pt/Ni as 3:1, 1:1 and 2:3 (denoted as Pt_3Ni_1, Pt_1Ni_1 and Pt_2Ni_3 in the context below), respectively. It can be seen that regardless of the Pt/Ni atomic ratios, the products all exhibited as chain-like structures composed by the attachment of near-spherical nanoparticles with mean diameters of 4~5 nm, which tended to cross-linked into networks. As shown in Figure 1(d), the three samples (Pt_3Ni_1, Pt_1Ni_1 and Pt_2Ni_3) possessed similar X-ray diffraction (XRD) patterns, which can be indexed to face-centered-cubic (fcc) phase. Rather surprisingly, no obvious peak shift was identified relative to the XRD pattern of the pure Pt nanoparticles obtained using similar process except the introduction of Ni precursor, which excludes the possibility of the alloyed structures. However, the diffractions from Ni were not observed. "Fluorescence effect" might contribute to the absent signal from Ni in the XRD pattern. It is known that the fluorescence effect exists for elements one to five place left of the target material in periodic table. Cu-Kα radiation is employed during the XRD characterization in our case, thus the strong florescence would lead to the high background to blanket the signals from Ni.

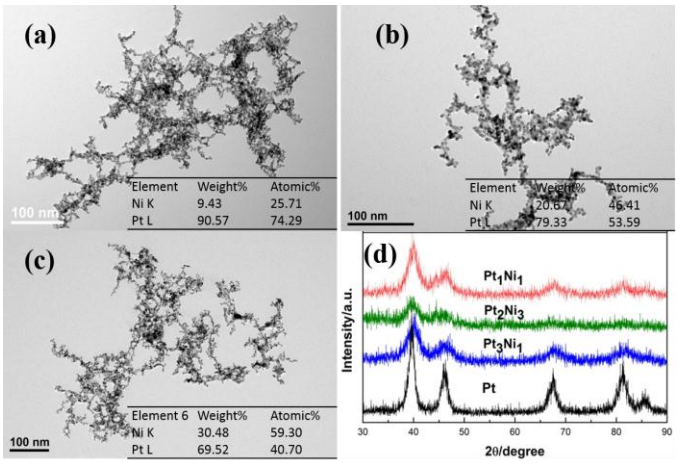

Figure 1. Broad view TEM images of (a) Pt_3Ni_1, (b)Pt_1Ni_1, and (c)Pt_2Ni_3, (d) the corresponding XRD patterns of Pt-Ni nanohybrids of various compositions and pure Pt nanoparticles produced by a similar procedure. The inserted tables show the composition data obtained from EDX results.

To figure out their detailed configurations, HRTEM measurement was employed. Figures 2(a) to 2(f) show the typical HRTEM images of Pt_3Ni_1, Pt_1Ni_1 and Pt_2Ni_3, respectively. The clearly identified grain boundary provides solid evidence for the nanoparticle attachment nature. The lattice fringes with spaces of 0.226 and 0.203 nm can be identified in all cases, consistent well with (111) planes of fcc-Pt (JCPDS 04-0802) and fcc-Ni (JCPDS 04-0850)[32], respectively. That is to say that the nanochains were assembled by the attachment of phase-segregated Pt and Ni nanoparticles instead of Pt-Ni nanoalloys. After detailed analysis, configuration schematic diagrams were built to illustrate the corresponding composition distribution of the chains in the images. It indicates that the Pt and Ni nanoparticles were arranged in a random manner. Much closer observation reveals that the nanoparticles were not attached physically, but interfacial fusion had occurred both among the homogeneous-particles (Pt-Pt and Ni-Ni) and among the heterogeneous-particles (Pt-Ni) as demonstrated by the enlarged images recorded on the interfacial regions. Thus, it is reasonable to infer that the Pt and Ni subunits might share a mixed interface or there might exist a small number of Pt-Ni bonds in the products despite of the phase-segregated structure feature. The interfacial atomic diffusion is not out of expectation since the alloying ability between Ni and Pt is extremely strong.[13, 33]

Then, it gives rise to another question on why the phase-segregated structure rather than the alloy was generated. In our case, the color of the reaction solution turned into black at about 180°C before the introduction of hydrazine hydrate ($N_2H_4 \cdot H_2O$). TEM and EDS characterization results reveal that the products collected at this stage mainly consisted of Pt nanoparticles (as shown in Figure S2 in the supporting information). Considering the much higher standard reduction potential of the $PtCl_6^{2-}$/Pt（E^{θ} = 0.375 eV vs. SHE）than that of Ni^{2+}/Ni (E^{θ}= -0.25 eV vs. SHE), it is easy to understand since ethylene glycol is a weak reducer. It is known that hydrazine hydrate ($N_2H_4 \cdot H_2O$) is a kind of strong reducing agent. Under refluxing, the introduction of $N_2H_4 \cdot H_2O$ led to continuous growth for Pt and fast nucleation and growth for Ni. Ni must have grown into nanoparticles before the Ni atoms had sufficient time to diffuse into the lattice of Pt. The separated nucleation-growth process for Pt and Ni produced the phase-segregated nanoparticles. The insufficient energy at relative low reaction temperature (＜200ºC) might be another possible reason to restrain the bulk alloying. The failure to obtain pure Pt chain-like structure in the absence of $NiCl_2$ as shown in Figure S1 indicates that Ni played a critical role on the growth of chain-like structure. We believe it was the dipole-dipole interaction worked. For magnetic Ni nanoparticles, they behaved like magnetic dipoles, which also induced the dipoles of the neighboring Pt nanoparticles. The strong and long range dipole-dipole interactions[34] organized the nanoparticles together. The linear arrangement is believed to can maximize the attraction of opposite magnetic poles.[35] Under refluxing, the interfacial atomic diffusion was facilitated, which made the adjacent particles fuse into each other and thus the chain-like structures were stabilized. The control experiment indicated that without the addition of PVP, the products exhibited as aggregates composed by irregular particles with sizes as large as ~ 50 nm (see Figure S3 in the supporting information). It is not out of the expectation since the PVP was reported as the classical surfactant to prevent the agglomeration of the nanoparticles.[36, 37] Scheme 1 depicts the formation mechanism of the phase-segregated Pt-Ni chain-like nanohybrids.

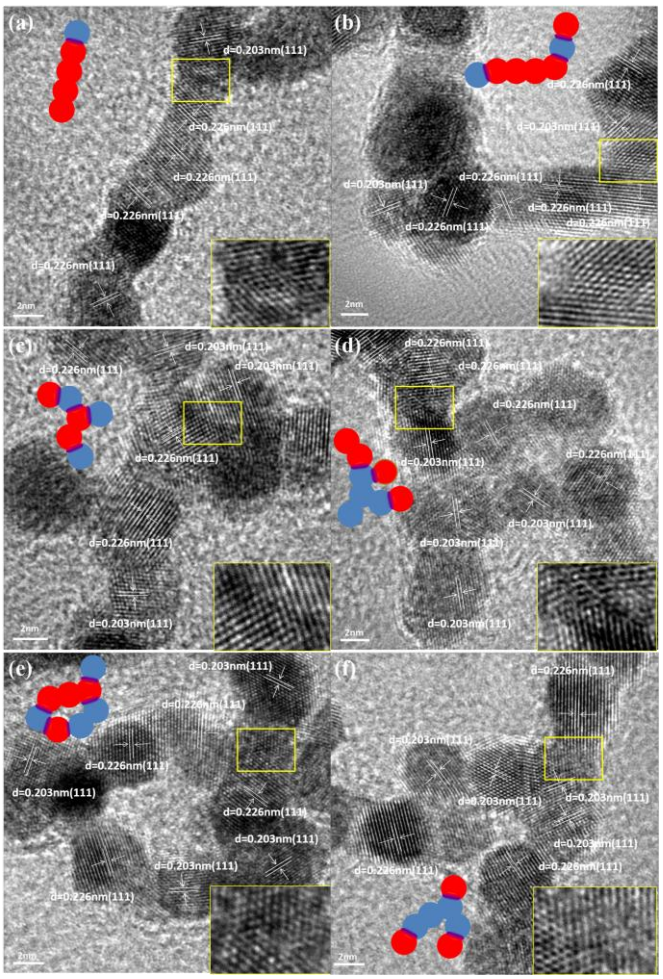

Figure 2. The HR-TEM images of (a, b) Pt_3Ni_1, (c, d) Pt_1Ni_1, (e, f) Pt_2Ni_3. The inserted schematic diagrams illustrate the configuration of Pt and Ni, with red and green ball representing Pt and Ni particles, respectively. The insert at the lower right corner of each HRTEM image is the corresponding amplified images recorded at the yellow framed regions, showing the detailed structure information at the Pt-Ni interfacial area.

To further examine the surface characteristics of the nanohybrids with different Pt/Ni atomic ratios, XPS measurements were performed. From the curves 1-3 in Figure 3(a), the Pt4f core-level spectra of the three samples all consisted of two peaks for metallic platinum centered at ~71 ($Pt4f_{7/2}$) and ~74 eV ($Pt4f_{5/2}$), respectively. No Pt^{2+}- and Pt^{4+}-related peaks were observed. The metallic Pt is believed to provide more active sites for methanol oxidation than ionic Pt species.[38] It is worth noting that in comparison with the pure Pt nanoparticles, the Pt4f core-level peaks of the as-prepared nanohybrids all shifted towards the lower binding energy side, with the negative shifts of about 0.18, 0.45 and 0.40 eV for Pt_3Ni_1, Pt_1Ni_1 and Pt_2Ni_3, respectively. In conjunction with the HR-TEM and XRD results, we can conclude that the electron transfer between Pt and Ni happened owing to the atomic diffusion at the interfaces. Due to the electronegativity difference between Pt (2.28) and Ni (1.91), the electron shift from Ni to Pt led to the downshift of the d-band center of Pt and thus the lowered binding energy. Obviously, the larger Pt-Ni interfacial area would facilitate the electron transfer. Since the contact possibility between Pt and Ni would be maximized when Pt : Ni approaches 1:1, the Pt 4f core-level peaks of Pt_1Ni_1 and Pt_2Ni_3 would be expected to shift more negatively than Pt_3Ni, consistent with the experimental data in our case.

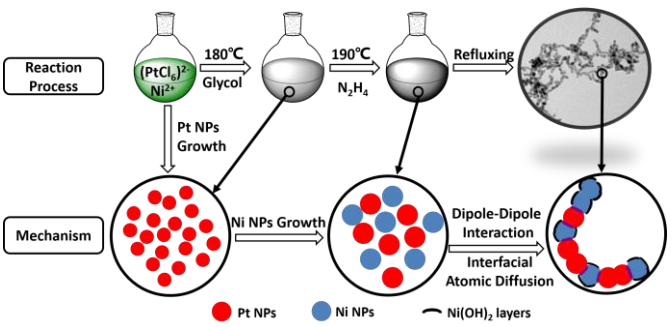

Scheme 1. The scheme illustration of the formation mechanism of the phase-segregated Pt-Ni chain-like nanohybrids.

The Ni2p spectra of the nanohybrids are shown in Figure 3(b). Generally, the structure of the Ni2p core-level spectra is complicated because of the presence of the broad satellite peaks (~860.9 eV and ~879.9 eV) adjacent to the main peaks, which are attributed to multi-electron excitation. Besides the shake-up peaks, both metallic Ni-related and $Ni(OH)_2$-related peaks can be clearly identified. According to the well-documented data,[39] the peaks at 852.5 eV are originated from metallic Ni and the peaks at 855.7 eV can be assigned to $Ni(OH)_2$. To further confirm the existence of $Ni(OH)_2$, we performed the cyclic voltammetry (CV) measurement in aqueous alkaline solutions. Typical electrochemical redox peaks are expected

owing to the electrochemical reaction between $Ni(OH)_2$ and NiOOH according to the following equation:

$Ni(OH)_2 + OH^- \leftrightarrow NiO(OH) + H_2O + e$

Figure S4 in the supporting information shows the CV curves of the Pt_2Ni_3 nanohybrids. The CV curves exhibit a broad cathodic current peak at around 0.3 V and an anodic current peak at around 0.4 V (vs. Ag/AgCl). The anodic current peak is related to the oxidation of nickel hydroxide to nickel oxyhydroxide while the cathodic one is associated with the reduced conversion of oxyhydroxide back to nickel hydroxide.[40]

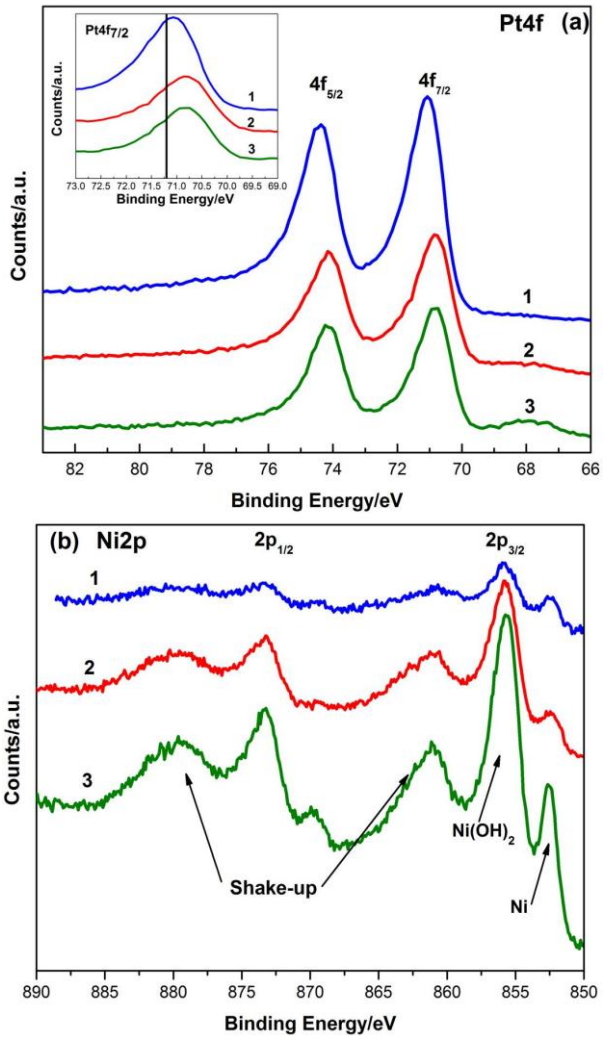

Figure 3. XPS spectra of Pt-Ni nanohybrids, spectra 1 to 3 correspond to Pt_1Ni_1, Pt_3Ni_1, and Pt_2Ni_3, respectively. (a) Pt 4f, (b) Ni 2p.

The electrocatalytic performance of the as-prepared Pt-Ni nanocatalysts towards MOR was studied by electrochemical cyclic voltammetry and chronoamperometry. For comparison, the pure Pt catalyst synthesized by the similar process as shown in Figure S1 was also examined. Figure 4(a) shows the CV curve of the as-prepared nanocatalysts recorded in 0.5mol/L H_2SO_4 without methanol from -0.2V to 1.0V at a sweep rate of 50 mV/s. The electrocatalytic currents were normalized to the mass of Pt. The curves of the nanohybrids resembled that of the pure Pt nanoparticles, showing well-defined hydrogen adsorption/desorption peaks in the potential region of -0.2V to 0.2V, the double-layer region from 0.20 to 0.40 V, and the metal oxidation/reduction peaks in the range of 0.4V to 0.8V. The electrochemically active surface area (EASA) was calculated on the basis of the integrated hydrogen desorption area, according to the equation EASA = $Q_H/(Q^H_{monolayer} \times W_{Pt})$, where Q_H is the total charge (μC) for hydrogen desorption, $Q^H_{monolayer}$ represents the charge density involved for hydrogen monolayer desorption from a smooth Pt surface (210 $\mu C/cm^2$) and W_{Pt} represents the Pt loading on the electrode.[41] The EASA values of Pt_3Ni_1, Pt_1Ni_1, Pt_2Ni_3 and pure Pt nanocatalysts were 13, 24, 9 and 5 m^2/g, respectively. The integrated hydrogen adsorption area shows that the EASAs of Pt_3Ni_1, Pt_1Ni_1, Pt_2Ni_3 were all higher than that of pure Pt, indicating more electrochemical active sites with the addition of Ni.

Figure 4(b) shows the typical CV curves of methanol electrooxidation on Pt-based catalysts tested in aqoeous solution containing 0.5mol/L H_2SO_4 + 1 mol/L CH_3OH. The overall shapes of the cyclic voltammograms were in good agreement with the previous literature. At potentials below 0.20 V, the oxidation current was negligible in all voltammograms because the surface Pt active sites were poisoned by CO_{ads}, an intermediate from dehydrogenation of methanol. With the potential increasing, the methanol oxidation began and well-defined anodic peaks were observed at about 0.70V (see Table 1) in the forward sweep. Onset potential of methanol oxidation and the forward anodic peak potential are the two major parameters to evaluate the catalytic performance.[42, 43] As can be seen in the inset of Figure 4(b), the onset potentials with the as-prepared Pt-Ni nanohybrids as the catalysts were all lower than that of the pure Pt, suggesting it was more favorable for methanol oxidation. Ni in the Pt-based catalysts are believed to significantly lower the onset potential through the synergistic effect, in which the adsorption of oxygenous species occurred at much lower potential on the additive Ni than that on Pt. The anodic peak current was also enhanced by the addition of Ni. The mass-normalized current density (as shown in Figure (d)) of the anodic peak on Pt_1Ni_1 nanocatalysts (136 mA/mg_{Pt}) was higher than that on Pt_3Ni_1 (62 mA/mg_{Pt}) and Pt_2Ni_3 (43 mA/mg_{Pt}) and as high as about 4 times of pure Pt (33 mA/mg_{Pt}). The area-normalized specific peak current density (as shown in Figure S5 and Figure 4d) of the Pt_1Ni_1 nanocatalysts (4.7 mA/cm^2) was also higher than those of the Pt_3Ni_1 (4.3 mA/cm^2) and the Pt_2Ni_3 (3.7 mA/cm^2), and was about 2 times higher than that of pure Pt (2.8 mA/cm^2). The results indicate that the addition of Ni enhanced the electrochemical activity of Pt.

Furthermore, the long-term stability and tolerant ability to CO intermediates were evaluated by the chronoamperometry measurements performed in 0.5mol/L H_2SO_4 + 1 mol/L CH_3OH at 0.70V. As shown in Figure 4(c), the current densities of all catalysts decayed rapidly at the initial stage, which might be due to the hydrogen adsorption and the double-layer discharge. The subsequent decay was believed to be caused by the adsorption of a small amount of CO on the catalyst surfaces during methanol electrooxidation.[44] Although the current continued to decay gradually, the nanohybrids all maintained a higher current density (normalized to the mass of Pt) than the pure Pt over the entire time range, demonstrating the prominent stability and tolerance to CO. Among the three samples, Pt_1Ni_1 exhibited the slowest current decay over time, confirming its excellent electrocatalytic performance.

Obviously, the phase-segregated Pt-Ni chain-like nanohybrids in our case were highly beneficial as anodic electrocatalysts for MOR relative to pure Pt, benefited by the following three aspects: (a) the lowered onset potential for the methanol oxidationreaction; (b) the higher mass activity and specific activity towards the methanol oxidation; (c) the enhanced long-term stability and resistance to CO poisoning. On the whole, the catalytic activities toward MOR followed the sequence of Pt_1Ni_1> Pt_2Ni_3~Pt_3Ni_1> pure Pt. The enhanced electrocatalytic performance probably could be attributed

to the so-called bifunctional mechanism. According to the XPS results, the electronic structure of Pt was modified by the electron transfer from Ni to Pt, which led to the downshifted d-band center of Pt and thus reduced the adsorption energies of CO on Pt. The existence of $Ni(OH)_2$ layers on the catalysts was also believed to play an important role in the improvement of the catalytic activity. It was reported that the OH species produced from the hydroxide layer could react with the CO_{ads} species on the Pt particles. The process can be described as the following equation: $NiOH_{ads} + PtCO_{ads} \rightarrow CO_2 + Pt + Ni + H^+ + e$.[18, 45] The desorption of CO_{ads} could recover the active sites on Pt. However, excess Ni loading would also lower the catalytic activity since the excess surface occupation by Ni would decrease the available Pt for MOR. The combination of the lowered d-band center and the efficient active sites endowed the Pt_1Ni_1 with the best catalytic performance.

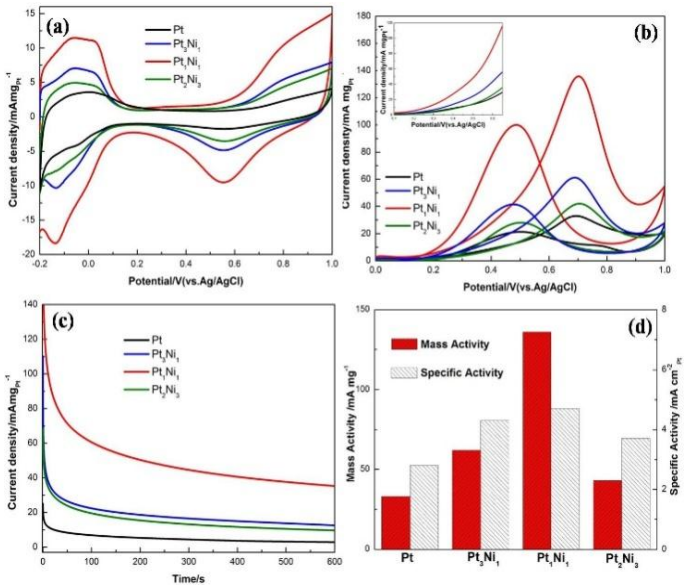

Figure 4. Cyclic voltammograms of Pt-Ni nanohybrids in (a) 0.5 mol/L H_2SO_4, (b) 0.5 mol/L H_2SO_4 + 1 mol/L CH_3OH, (c) Chronoamperometry curves of Pt-Ni nanohybrids in 0.5 mol/L H_2SO_4 + 1 mol/L CH_3OH at 0.7 V. (d) Comparison of mass and area specific activities of the four catalysts for methanol oxidation. The insert in (b) is the amplified part of the CVs at low potential range. The scanning rate in all the cases is 50 mV/s.

Table 1. Comparison of the Catalytic Activity of the Pt-Ni Catalysts for Methanol Oxidation

Catalyst	EASA /$m^2\ g^{-1}$	Onset Potential /V	Specific Activity /mA cm^{-2}	Mass Activity /mA mg_{Pt}^{-1}
Pt	13	0.39	2.8	33
Pt_3Ni_1	24	0.29	4.3	62
Pt_1Ni_1	9	0.25	4.7	136
Pt_2Ni_3	5	0.34	3.7	43

Conclusions

The phase-segregated Pt-Ni chain-like nanohybrids were synthesized via a modified polyol process with the assistance of small amount of PVP. HRTEM characterizations show that the nanohybrids were composed by the attachment of the Ni and Pt nanoparticles in a random manner with the nature of interfacial atomic fusion. The separated nucleation-growth process for Pt and Ni and the relative low reaction temperature prevented the diffusion of Ni atoms into the bulk Pt, which guaranteed the phase-segregated structure. The dipole-dipole interaction was believed to responsible for the formation of the chain-like structure. XPS results reveal the modified electron structure of Pt owing to the charge transfer from Ni at the interfacial region. The electrocatalytic performance for MOR was evaluated by the cyclic voltammogrametry and chronoamperometry. The nanohybrids exhibit both higher electrocatalytic activities and improved CO tolerance relative to the pure Pt nanoparticles synthesized under similar conditions. The activity and the stability both followed the sequences of Pt_1Ni_1> Pt_3Ni_1~Pt_2Ni_3 >> pure Pt. We believe the modified electronic structures and the existence of nickel hydroxide both contributed to the improved electocatalytic performance.

Acknowledgements

The project was supported by National Natural Science Foundation of China (21173015), the National Key Basic Research Program of China (973) (2010CB934700).

Notes and References

School of Chemistry and Environment, Beihang University, Beijing 100191, PR China. Email: dfzhang@buaa.edu.cn; guolin@buaa.edu.cn.

† Electronic Supplementary Information (ESI) available:

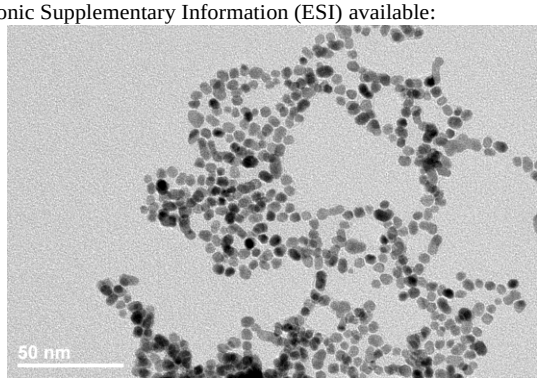

Figure S1. TEM image of pure Pt nanoparticles obtained under similar conditions except for the introduction of Ni precursor.

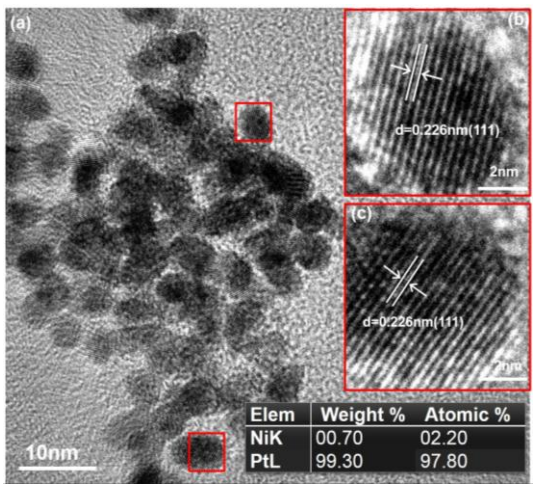

Figure S2. (a) TEM image of the products obtained at about 180°C, (b) and (c) are the corresponding amplified images recorded at the red framed

nanoparticles, showing the lattice spaces of 0.226nm, consistent well with (111) planes of fcc-Pt. The insert table illustrates the composition of the products with overwhelming majority Pt.

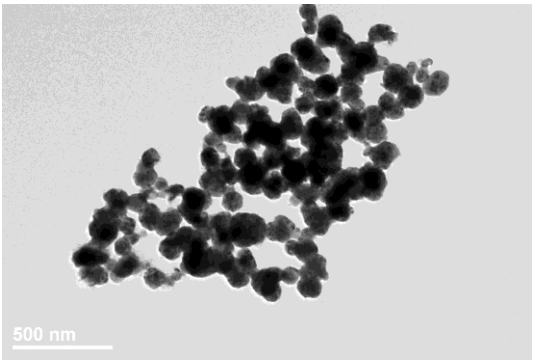

Figure S3. TEM image of the products obtained using similar process except for the addition of PVP.

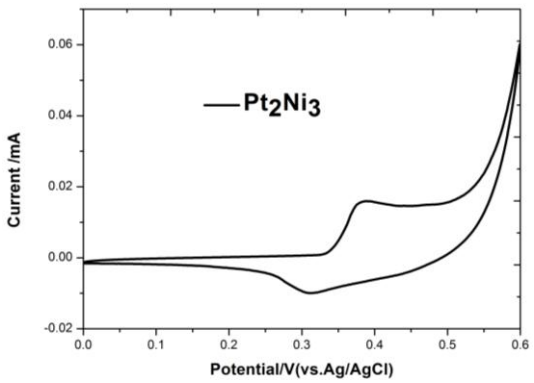

Figure S4. The CV curves of the as-prepared Pt_2Ni_3 nanohybrids cycled in 1 M KOH aqueous solution between 0.0 and 0.6 V (vs Ag/AgCl) at the sweeping rate of 50 mV/s.

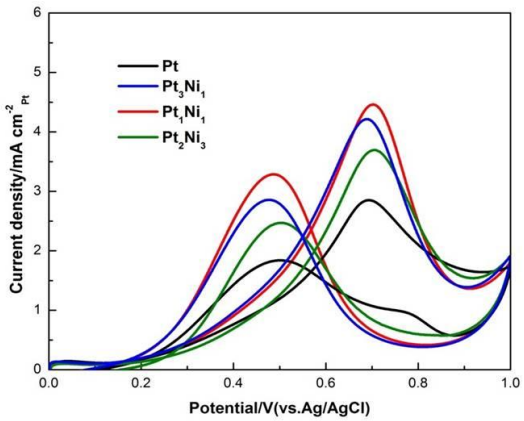

Figure S5. Cyclic voltammograms of Pure Pt and Pt-Ni nanohybrids in 0.5 mol/L H_2SO_4 + 1 mol/L CH_3OH. Scanning rate is 50 mV/s.

See DOI: 10.1039/b000000x/

1. G. A. Somorjai, *Chem. Rev.*, 1996, **96**, 1223-1235.
2. H. Zhang, M. Jin and Y. Xia, *Chem. Soc. Rev.*, 2012, **41**, 8035-8049.
3. S. H. Noh, M. H. Seo, J. K. Seo, P. Fischer and B. Han, *Nanoscale*, 2013, **5**, 8625-8633.
4. S. R. Brankovic, J. McBreen and R. R. Adzic, *Surf. Sci.*, 2001, **479**, L363-L368.
5. S. R. Brankovic, J. X. Wang, Y. Zhu, R. Sabatini, J. McBreen and R. R. Adzic, *J. Electroanal. Chem.*, 2002, **524**, 231-241.
6. K. Sasaki, Y. Mo, J. X. Wang, M. Balasubramanian, F. Uribe, J. McBreen and R. R. Adzic, *Electrochim. Acta*, 2003, **48**, 3841-3849.
7. A. Schlapka, M. Lischka, A. Groß, U. Käsberger and P. Jakob, *Phys. Rev. Lett.*, 2003, **91**.
8. V. R. Stamenkovic, B. Fowler, B. S. Mun, G. Wang, P. N. Ross, C. A. Lucas and N. M. Markovic, *Science*, 2007, **315**, 493-497.
9. T. G. Kelly and J. G. Chen, *Chem. Soc. Rev.*, 2012, **41**, 8021-8034.
10. B. Hammer, L. B. Hansen and J. K. Nørskov, *Phys. Rev. B*, 1999, **59**, 7413-7421.
11. W. Du, Q. Wang, D. Saxner, N. A. Deskins, D. Su, J. E. Krzanowski, A. I. Frenkel and X. Teng, *J. Am. Chem. Soc.*, 2011, **133**, 15172-15183.
12. D. V. Esposito, S. T. Hunt, Y. C. Kimmel and J. G. Chen, *J. Am. Chem. Soc.*, 2012, **134**, 3025-3033.
13. T. C. Deivaraj, W. Chen and J. Y. Lee, *J. Mater. Chem.*, 2003, **13**, 2555.
14. X. Teng, S. Maksimuk, S. Frommer and H. Yang, *Chem. Mater.*, 2007, **19**, 36-41.
15. C. Wang, D. van der Vliet, K. L. More, N. J. Zaluzec, S. Peng, S. Sun, H. Daimon, G. Wang, J. Greeley, J. Pearson, A. P. Paulikas, G. Karapetrov, D. Strmcnik, N. M. Markovic and V. R. Stamenkovic, *Nano Lett.*, 2011, **11**, 919-926.
16. J. Suntivich, Z. Xu, C. E. Carlton, J. Kim, B. Han, S. W. Lee, N. Bonnet, N. Marzari, L. F. Allard, H. A. Gasteiger, K. Hamad-Schifferli and Y. Shao-Horn, *J. Am. Chem. Soc.*, 2013, **135**, 7985-7991.
17. C. Xu, P. k. Shen and Y. Liu, *J. Power Sources*, 2007, **164**, 527-531.
18. E. Formo, Z. Peng, E. Lee, X. Lu, H. Yang and Y. Xia, *J. Phys. Chem. C*, 2008, **112**, 9970-9975.
19. J. J. Pietron, M. B. Pomfret, C. N. Chervin, J. W. Long and D. R. Rolison, *J. Mater. Chem.*, 2012, **22**, 5197.
20. J. W. Long, R. M. Stroud, K. E. Swider-Lyons and D. R. Rolison, *J. Phys. Chem. B*, 2000, **104**, 9772-9776.
21. M. Inoue, T. Nishimura, S. Akamaru, A. Taguchi, M. Umeda and T. Abe, *Electrochim. Acta*, 2009, **54**, 4764-4771.
22. R. Mu, Q. Fu, H. Xu, H. Zhang, Y. Huang, Z. Jiang, S. Zhang, D. Tan and X. Bao, *J. Am. Chem. Soc.*, 2011, **133**, 1978-1986.
23. D. Wu, Z. Zheng, S. Gao, M. Cao and R. Cao, *Phys. Chem. Chem. Phys.*, 2012, **14**, 8051-8057.
24. Q. Y. Lu, B. Yang, L. Zhuang and J. T. Lu, *J. Phys. Chem. B*, 2005, **109**, 8873-8879.
25. E.-Y. Ko, E. D. Park, K. W. Seo, H. C. Lee, D. Lee and S. Kim, *Catal. Lett.*, 2006, **110**, 275-279.
26. E. Y. Ko, E. D. Park, H. C. Lee, D. Lee and S. Kim, *Angew. Chem. Int. Ed. Engl.*, 2007, **46**, 734-737.
27. C. Wang, N. M. Markovic and V. R. Stamenkovic, *ACS Catal.*, 2012, **2**, 891-898.
28. C. Wang, M. Chi, G. Wang, D. van der Vliet, D. Li, K. More, H.-H. Wang, J. A. Schlueter, N. M. Markovic and V. R. Stamenkovic, *Adv. Funct. Mater.*, 2011, **21**, 147-152.
29. C. Wang, M. Chi, D. Li, D. Strmcnik, D. van der Vliet, G. Wang, V. Komanicky, K. C. Chang, A. P. Paulikas, D. Tripkovic, J. Pearson, K. L. More, N. M. Markovic and V. R. Stamenkovic, *J. Am. Chem. Soc.*, 2011, **133**, 14396-14403.
30. M. Chen, B. Wu, J. Yang and N. Zheng, *Adv. Mater.*, 2012, **24**, 862-879.
31. H. Chen, D. Wang, Y. Yu, K. A. Newton, D. A. Muller, H. Abruna and F. J. DiSalvo, *J. Am. Chem. Soc.*, 2012, **134**, 18453-18459.
32. X. Huang, E. Zhu, Y. Chen, Y. Li, C. Y. Chiu, Y. Xu, Z. Lin, X. Duan and Y. Huang, *Adv. Mater.*, 2013, **25**, 2974-2979.

33. J. Zhang, H. Yang, J. Fang and S. Zou, *Nano Lett.*, 2010, **10**, 638-644.
34. S. A. Iakovenko, A. S. Trifonov, M. Giersig, A. Mamedov, D. K. Nagesha, V. V. Hanin, E. C. Soldatov and N. A. Kotov, *Adv. Mater.*, 1999, **11**, 388-392.
35. Z. Tang, N. A. Kotov and M. Giersig, *Science*, 2002, **297**, 237-240.
36. Y. Xiong, I. Washio, J. Chen, H. Cai, Z.-Y. Li and Y. Xia, *Langmuir*, 2006, **22**, 8563-8570.
37. O. D. Lyons, N. E. Musselwhite, L. M. Carl, K. A. Manbeck and A. L. Marsh, *Langmuir*, 2010, **26**, 16481-16485.
38. Y. Hu, P. Wu, Y. Yin, H. Zhang and C. Cai, *Appl. Catal. B: Environ*, 2012, **111-112**, 208-217.
39. T.-Y. Jeon, S. J. Yoo, Y.-H. Cho, K.-S. Lee, S. H. Kang and Y.-E. Sung, *J. Phys. Chem. C*, 2009, **113**, 19732-19739.
40. K. Watanabe, T. Kikuoka and N. Kumagai, *J. Appl. Electrochem.*, 1995, **25**, 219-226.
41. A. C. Ferrandez, S. Baranton, J. Bigarre, P. Buvat and C. Coutanceau, *Langmuir*, 2012, **28**, 17832-17840.
42. Z. Zhang, Y. Wang and X. Wang, *Nanoscale*, 2011, **3**, 1663-1674.
43. J. Xu, X. Liu, Y. Chen, Y. Zhou, T. Lu and Y. Tang, *J. Mater. Chem.*, 2012, **22**, 23659.
44. L. X. Ding, A. L. Wang, G. R. Li, Z. Q. Liu, W. X. Zhao, C. Y. Su and Y. X. Tong, *J. Am. Chem. Soc.*, 2012, **134**, 5730-5733.
45. B. Habibi and E. Dadashpour, *Int. J. Hydrogen Energy*, 2013, **38**, 5425-5434.